RSC Advances

PAPER

View Article Online
View Journal | View Issue

Cite this: *RSC Adv.*, 2026, **16**, 22829

Study of solid-state synthesized $Pr_{0.55}Sr_{0.45}Mn_{1-x}Cr_xO_3$ perovskites with $x = 0.0$, 0.05, 0.1 and 0.15: Rietveld analysis and magnetic and magnetocaloric properties for magnetic refrigeration applications

A. Selmi, *[a] H. Ayed,[a] Malek Gassoumi,[a] W. Cheikhrouhou-Koubaa,[b] E. K. Hlil[c] and Abdelaziz Bouazizi[a]

In the current study, the structural (X-ray diffraction (XRD)), magnetic, critical behavior and magnetocaloric properties of polycrystalline $Pr_{0.55}Sr_{0.45}Mn_{1-x}Cr_xO_3$ manganite samples (with $x = 0.0$, 0.05, 0.1 and 0.15) were investigated. All our samples were prepared from the stoichiometric powder mixtures of binary oxides *via* solid-state reactions at high temperatures. The compounds crystallized in an orthorhombic structure with the *Pnma* space group, according to the Rietveld refinement of the XRD pattern. All the samples exhibited a second-order FM-to-PM phase transition, according to the temperature and field-dependent magnetization measurements; however, the Curie temperature (T_C) value decreased from 300 K to 275 K, as the Cr (% x) content increased from 0.00 to 0.15. Using Maxwell thermodynamic relations, the magnetocaloric effect (MCE) in terms of maximum entropy change ($-\Delta S_M^{max}$) and relative cooling power (RCP) was calculated with isothermal magnetization data around T_C. In a magnetic field shift of 5 T, the highest values of the magnetic entropy change ($-\Delta S_M^{max}$) were determined to be 3.8 J kg^{-1} K^{-1}, 3.63 J kg^{-1} K^{-1}, 3.87 J kg^{-1} K^{-1}, and 2.55 J kg^{-1} K^{-1} for $x = 0.0$, $x = 0.05$, $x = 0.1$, and $x = 0.15$, respectively. For $x = 0.0$, $x = 0.05$, $x = 0.1$, and $x = 0.15$ at 5 T, the highest value of the relative cooling power RCP was found to be 247 J kg^{-1}, 254.1 J kg^{-1}, 205.1 J kg^{-1}, and 201 J kg^{-1}, respectively. The RCP value of 254.1 J kg^{-1} (5% of chromium) was equivalent to 58% of the RCP value of gadolinium metal. Technically, the developed material is highly promising for magnetic refrigeration because of these significant values.

Received 11th March 2026
Accepted 18th April 2026

DOI: 10.1039/d6ra02079h

rsc.li/rsc-advances

1 Introduction

Perovskite manganites with the general formula of $RE_{1-x}AE_xMnO_3$ (RE = rare earth ions such as La^{3+}, Pr^{3+}, Nd^{3+}, and Sm^{3+} and AE = alkaline earth ions such as Sr^{2+}, Ba^{2+}, and Bi^{2+}) have drawn a lot of research interest in the recent three decades owing to their unique physical characteristics, including phase separation, charge and orbital ordering, metal-to-insulator transition, and magnetocaloric effects.[1] We focused on a family of perovskite compounds in this work.

Recently, perovskite manganite compounds have been employed in a variety of applications, such as magnetic refrigeration systems,[2] magnetoresistance devices,[3,4] and high-efficiency photovoltaic solar cells,[5] which showed that manganite-family perovskites with different doping atoms have extremely high relative cooling power (RCP), making them suitable for clean refrigeration source applications.[2] Since the discovery of magneto-caloric effects (MCEs) by Warburg in 1881,[6] they have been extensively studied, becoming the foundation of the so-called "magnetic refrigeration".

Due to its large magnetic entropy change around room temperature, gadolinium (Gd) is a well-known standard among the magnetocaloric materials. However, the relatively high cost of Gd limits its large-scale technological applications. As a result, substantial effort has been put into developing low-cost alternatives, particularly rare-earth-based perovskite manganites, which exhibit fascinating magnetocaloric properties. The main objective is to identify materials with magnetic entropy change ($-\Delta S_M^{max}$) and relative cooling power (RCP) values comparable to those of Gd while significantly reducing the material cost. In this case, manganite perovskites constitute

[a]*Equipe Dispositifs Electroniques Organiques et Photovoltaïque Moléculaire, Laboratoire de la Matière Condensée et des Nanosciences, Faculté des Sciences de Monastir, Université de Monastir, Avenue de l'environnement, 5019 Monastir, Tunisia. E-mail: bohmids@gmail.com*

[b]*LT2S Lab, Digital Research Centre of Sfax, Sfax Technopark, BP 275, 3021 Sakiet-Ezzit, Tunisia*

[c]*Univ. Grenoble Alpes, CNRS, Grenoble INP, Institut N'eel, 38000 Grenoble, France*

a suitable and economically viable class of materials for magnetic refrigeration applications.

Numerous studies have examined the crucial character of manganites close to a PM-to-FM phase transition.[7–33] Several methods of changing the physical characteristics of perovskite manganite $RE_{1-x}AE_xMnO_3$, for example, replace the trivalent rare earth ions (RE^{3+}) in the perovskite structure with a divalent element (AE^{2+}). A mixed valence of manganese Mn^{3+} and Mn^{4+} appears as a result of the partial substitution of RE^{3+}. This valence state is at the base of the changes in the physical properties of these perovskite manganites, in particular the appearance of a ferromagnetic (FM) order of the spins of the Mn ions, following which the electron e_g becomes itinerant and can hop from a Mn cation, *via* the oxygen anion, to another manganese having an empty e_g band. The strong relationship between structural, electrical, and magnetic properties is one of the essential features of manganites. The double exchange (DE) mechanism, first proposed by Zener in 1951, explains this association.[34] The replacement of rare earth elements has an indirect effect on the conduction mechanism, affecting the bandwidth and angle of the connection between the neighbouring manganese ions, according to several recent scientific studies[35–37] on manganites. Another way is to study the impacts of Mn doping by other elements, which is interesting since it is undeniable that Mn ions play a significant role in the double exchange interaction. Over the last few years, many research projects[38–49] have been conducted to comprehend the impact of replacing manganese at the B-site with a transition element. It has been demonstrated that the addition of a transition metal with an electronic configuration distinct from Mn should result in an important change in both Mn and the configurations of the substituent elements. Therefore, the conduction mechanism is directly impacted by the replacement of Mn, making it possible to more effectively modify the physical characteristics of the manganite systems. Additionally, the replacement of trivalent and tetravalent elements for Mn results in an increase in resistivity and a drop in transition temperature (T_C), and magnetism. However, the type of replacement elements mostly determines the precise effect. Chromium is one of these elements that affects the structural and magnetic characteristics of manganites. The doping of Mn by magnetic Cr has been cited in earlier studies,[50–55] and both investigations show that the inclusion of Chromium in both systems has comparable outcomes, specifically a drop in the temperature of the magnetic transition from the FM state to the PM state as the rate of substitution (x) increases. Additionally, the Mn–O–Mn networks are impacted by the substitution of Mn sites by other elements,[56,57] by the strong electron–phonon interaction known as the Jahn–Teller effect,[58] and the double-exchange (DE) interaction linking Mn^{3+}/Mn^{4+} ions.[59] The characteristics of the magnetocaloric effect are explained by these considerations. One of the manganites that has been investigated the most is $Pr_{1-x}Sr_xMnO_3$, which exhibits a $-\Delta S_M^{max}$ value around 3 J kg^{-1} K^{-1}under an applied magnetic field of 5 T and passes through a paramagnetic metal-to-ferromagnetic metal transition around $T_C \approx 301$ K.[60] This combination may undergo a ferromagnetic transition at ambient temperature with $-\Delta S_M^{max}$ greater than 4 J kg^{-1} K^{-1}, by partially substituting Mn ions with other transition metal ions, such as Chromium (M = Cr).

Magnetocaloric manganites have been extensively studied, but enhancing their performance remains challenging. The magnetocaloric response is actually greatly influenced by various parameters, including doping type, concentration, and structural distortions. Therefore, further research is still required to explore alternative replacement procedures and compositional tuning in order to achieve improved characteristics. An alternative and effective method is to study Cr substitution in $Pr_{0.55}Sr_{0.45}MnO_3$ in order to better understand the relationship between structure, magnetism, and magnetocaloric performance, as well as to identify materials that are suitable for magnetic refrigeration near ambient temperature.

The structural, magnetic, and magnetocaloric characteristics of the series of manganite compounds $Pr_{0.55}Sr_{0.45}Mn_{1-x}Cr_xO_3$ with $x = 0.0$, 0.05, 0.1, and 0.15 were thoroughly examined in this work. The Rietveld method of analysing X-ray diffraction diagrams allowed for the precise determination of the structural characteristics of samples. To do this, we thoroughly examined the magnetocaloric effect and calculated the relative cooling power (RCP), a crucial performance indicator.

2 Experimental details

$Pr_{0.55}Sr_{0.45}Mn_{1-x}Cr_xO_3$ polycrystalline samples ($x = 0.0$, 0.05, 0.1, and 0.15) were prepared using the traditional solid-state reaction method. As starting materials, high-purity precursor powders (≥99.9% purity) of Pr_6O_{11}, $SrCO_3$, MnO_2, and Cr_2O_3 were weighed in accordance with the necessary stoichiometric ratios. To guarantee excellent homogeneity and uniform distribution of the contents, the powders were first combined and extensively ground in an agate mortar for several hours.

To eliminate volatile species and initiate solid-state reactions, the combined powders were first calcined in air at 900 °C for 24 hours. To enhance phase formation, the powders were reground after naturally cooling and then calcined again for 24 hours at 1100 °C. Then, the resultant powders were finely milled and compressed under uniaxial pressure into cylindrical pellets with a thickness of about 1 mm. In order to improve the crystallinity, density, and phase purity, the pellets were then sintered in air for 12 hours at high temperatures of 1200 °C and 1300 °C. In between sintering steps, the pellets were reground.[61,62] The samples were furnace-cooled to room temperature after all thermal treatments were carried out in an ambient air environment.

Using a PANalytical X'Pert Pro diffractometer with Cu-Kα radiation ($\lambda = 1.5406$ Å), the phase purity, crystal structure, and lattice parameters were examined by powder X-ray diffraction (XRD) at ambient temperature. To guarantee a high signal-to-noise ratio, the diffraction data were gathered in the 2θ range of 10–80° with a step size of 0.02° and a suitable counting duration per step. Structural analysis was performed by the standard Rietveld method[63–65] using the FullProf software.

A vibrating sample magnetometer (VSM) was used to measure magnetic fields up to 5 T. Field-cooled (FC) protocols were used to record the temperature-dependent magnetization

($M(T)$) in the 20–400 K temperature range. At certain temperatures near the magnetic transition region, isothermal magnetization curves $M(H)$ were recorded with magnetic fields ranging from 0 to 5 T.

Using the Maxwell thermodynamic relation, the magnetic entropy change (ΔS_M) was calculated from the isothermal magnetization data as follows:

$$\Delta S_M(T,H) = \int_0^{H_{max}} \left(\frac{\partial M}{\partial T}\right)_H dH.$$

In actuality, discrete $M(H)$ curves acquired at various temperatures were used to quantitatively determine ΔS_M. The full width at half maximum (δT_{FWHM}) of the $\Delta S_M(T)$ curve multiplied by the maximum entropy change was used to calculate the relative cooling power (RCP).

3 Results and discussion

3.1 Structural analysis

The X-ray diffraction pattern of $Pr_{0.55}Sr_{0.45}Mn_{1-x}Cr_xO_3$ with $x =$ 0.0, 0.05, 0.1, and 0.15 at room temperature is shown in Fig. 1. The XRD patterns showing sharp, well-defined peaks reveal a completely crystalline phase of $Pr_{0.55}Sr_{0.45}Mn_{1-x}Cr_xO_3$ with a distinct orthorhombic phase with the *Pnma* space group. The excellent quality and single-phase of the elaborated samples were demonstrated by the absence of secondary-phase-corresponding peaks (no impurity). The structural data are analysed by the Rietveld method using the FullProf program[63,64,66] to gain an improved understanding of the structural characteristics of the orthorhombic phase.

The goodness-of-fit parameter χ^2 and the reliability factors R_p and R_{wp}, which quantify the differences between the calculated and observed diffraction patterns, were used to evaluate the quality of the Rietveld refinement. The lattice parameters a, b, and c, scale factor, zero shift, atomic locations, and isotropic displacement parameters were among the structural and profile characteristics that were adjusted during the refinement process. A pseudo-Voigt function was used to fit the peak profiles, and a polynomial function was used to describe the background. There is good agreement between the calculated and experimental data, as seen by the obtained χ^2 values being near the predicted range. Lattice parameters, unit cell volume, atomic locations (x, y, z) for all atoms (Pr/Sr, Mn/Cr, O_1, and O_2) with their estimated standard deviations, and computed bond lengths and bond angles with corresponding errors are all included in Table 1, which summarizes all revised structural and reliability metrics. A thorough assessment of the refining quality is also provided by agreement factors, including Bragg R-factor, R_f-factor, R_e, R_p, R_{wp}, and χ^2.

Additionally, the Debye–Scherrer formula was used to obtain the average crystallite size D_{C-S} from the primary peak of the XRD data:

$$D_{C-S} = \frac{k \times \lambda}{\beta \times \cos\ \theta},$$

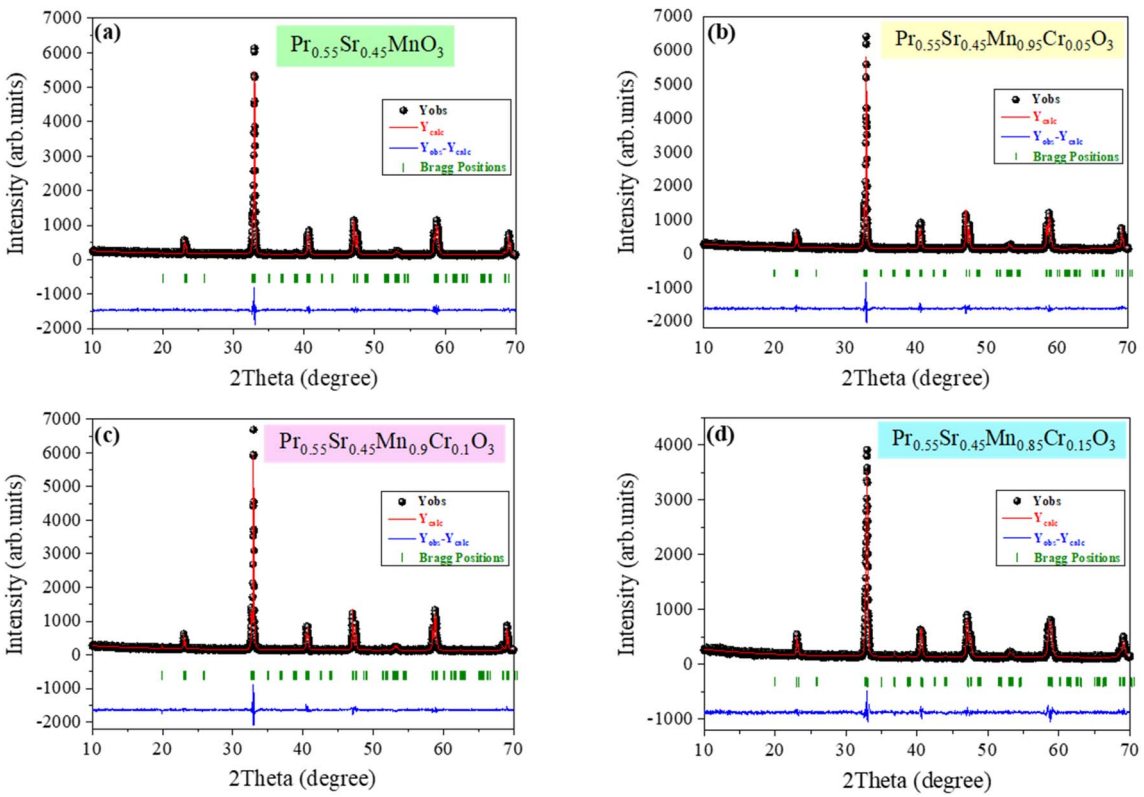

Fig. 1 X-ray powder diffraction patterns and refinement at room temperature for $Pr_{0.55}Sr_{0.45}Mn_{1-x}Cr_xO_3$ ((a) $x = 0$, (b) $x = 0.05$, (c) $x = 0.1$ and (d) $x = 0.15$) showing the calculated, observed, and difference intensities along the Bragg positions (vertical bars in green).

Table 1 Refined structural parameters of $Pr_{0.55}Sr_{0.45}Mn_{1-x}Cr_xO_3$ at room temperature

X	0	0.05	0.10	0.15
Symmetry	Orthorhombic	Orthorhombic	Orthorhombic	Orthorhombic
Space group	*Pnma*	*Pnma*	*Pnma*	*Pnma*
Cell parameters				
a (Å)	5.4409(3)	5.4372(2)	5.43928(20)	5.4455(5)
b (Å)	7.6558(3)	7.6502(3)	7.6548(3)	7.6514(6)
c (Å)	5.4807(2)	5.48076(19)	5.48331(17)	5.4739(5)
V (Å^3)	228.296(0.018)	227.976(0.015)	228.305(0.013)	228.073(0.035)
Pr/Sr at. positions				
X	0.0048(8)	0.00558(2)	0.0060(3)	0.0052(8)
Y	0.2500(0)	0.2500(0)	0.2500(0)	0.2500(0)
Z	0.9876(3)	0.9937(1)	0.9924(2)	0.9935(6)
Mn/Cr at. positions				
X	0.0000(0)	0.0000(0)	0.0000(0)	0.0000(0)
Y	0.0000(0)	0.0000(0)	0.0000(0)	0.0000(0)
Z	0.5000(0)	0.5000(0)	0.5000(0)	0.5000(0)
O_1at. positions				
X	0.4900 (0)	0.5143(1)	0.525(2)	0.4960(4)
Y	0.2500(0)	0.2500(0)	0.2500(0)	0.2500(0)
Z	0.0200(0)	0.0231(6)	0.034(1)	0.0522(9)
O_2at. positions				
X	0.281(0)	0.2235(6)	0.2457(2)	0.3154(3)
Y	0.0153(3)	0.0186(3)	0.0173(5)	0.0021(4)
Z	0.2950(0)	0.2332(7)	0.232(3)	0.2963(6)
Structural parameters				
$\langle d_{Mn_1-O_2}\rangle$ (Å)	2.0623(2)	1.9129(4)	1.9685(5)	1.9084(4)
$\langle \theta_{Mn_1-O_2-Mn_1}\rangle$ (°)	173.24(4)	168.21(9)	168.22(4)	154.74(5)
$\langle d_{Mn_2-O_2}\rangle$ (Å)	1.8057(7)	1.9676(6)	1.9136(8)	2.0477(4)
$\langle \theta_{Mn_2-O_2-Mn_2}\rangle$ (°)	173.24(4)	168.21(9)	168.22(4)	154.74(5)
$\langle d_{Mn_1-O_1}\rangle$ (Å)	1.9494(5)	1.9354(5)	1.9366(1)	1.9342(7)
$\langle \theta_{Mn_1-O_1-Mn_1}\rangle$ (°)	158.09(9)	162.35(5)	162.35(7)	162.93(2)
Agreement factors				
Bragg R-factor	3.79	5.55	5.86	4.69
R_f-factor	7.52	10.1	10.3	6.18
R_e (%)	16.4	16.5	17.0	17.6
R_p (%)	30.5	31.7	33.6	33.1
R_{wp} (%)	20.5	20.7	21.8	22.4
χ^2 (%)	1.56	1.57	1.64	1.63
D_{C-S}(nm)	78	50.6	48.6	30.1

where k indicates a dimensionless constant ($k = 0.9$), β defines the peak half-height width, and θ represents the peak Bragg angle.

A thorough comprehension of the structural and functional characteristics intrinsic to our $Pr_{0.55}Sr_{0.45}Mn_{1-x}Cr_xO_3$ compound series (where $x = 0.0$, 0.05, 0.1, and 0.15) requires a careful examination of the crystallographic parameters, especially the manganese–oxygen $\langle d_{Mn-O}\rangle$ distances bond and the inter-octahedral $\langle \theta_{Mn-O-Mn}\rangle$ angles.

The size and degree of deformation of the MnO_6 octahedra are directly indicated by the $\langle d_{Mn-O}\rangle$ interatomic distances. In the $Pr_{0.55}Sr_{0.45}Mn_{1-x}Cr_xO_3$ structure, the substitution of Mn by chromium Cr significantly changes the average oxidation state of the manganese ions, resulting in the introduction of certain structural stresses. The Jahn–Teller effect, which is usually connected to the presence of Mn^{3+} cations, is likewise very sensitive to these ensuing variations in $\langle d_{Mn-O}\rangle$ bond lengths. The electrical asymmetry of these ions forces the octahedra to elongate or compress, which is crucial in establishing the local structural environment.

At the same time, the connectivity and coupling effectiveness between neighboring MnO_6 octahedra are determined by the $\langle \theta_{Mn-O-Mn}\rangle$ bond angles. The amount of octahedral inclination is directly influenced by the degree of chromium substitution. The double-exchange (DE) process of Mn^{3+}/Mn^{4+} that drives the

observed ferromagnetism in these manganites is crucially mediated by this tilting, making it extremely significant.

In particular, the orbital overlap is maximized when the $\langle\theta_{Mn-O-Mn}\rangle$ angle gets closer to the optimal 180°, which improves the charge carrier mobility and fortifies the magnetic interactions.

The complicated local structural distortions caused by Cr inclusion at the Mn site are responsible for the non-monotonic evolution of the average $\langle d_{Mn-O}\rangle$ bond lengths and $\langle\theta_{Mn-O-Mn}\rangle$ bond angles with the increasing Cr substitution. As Cr doping has non-uniform effects on the Jahn–Teller distortion, octahedral tilting, and $\langle d_{Mn-O}\rangle$ bond covalency in perovskite manganites, it does not always result in a linear structural response. The coexistence of Cr^{3+} and Mn^{3+}/Mn^{4+} ions causes local strain oscillations and alters the distortion of MnO_6 octahedra, leading to small irregular changes in bond angles and lengths. These minor alterations are in line with the findings from comparable Cr-doped manganite systems and demonstrate the orthorhombic *Pnma* structure's high sensitivity to compositional disorder and local lattice effects.

In conclusion, examining the simultaneous changes in $\langle d_{Mn-O}\rangle$ distances controlled by the Jahn–Teller effect and substitution and the $\langle\theta_{Mn-O-Mn}\rangle$ angles, which determine the effectiveness of the double-exchange pathway, is crucial to understanding the magnetic properties seen in $Pr_{0.55}Sr_{0.45}Mn_{1-x}Cr_xO_3$.

3.2 Magnetic properties

The temperature dependence of the magnetization ($M(T)$), under an applied magnetic field $\mu_0H = 0.05$ T, for all our samples, is displayed in Fig. 2(a). We plotted in Fig. 2(b) the magnetization as a function of temperature under a weak applied field of 0.05 T, with the dM/dT curve used to determine the minimum temperature (T_c) of the parent compound curve, clearly demonstrating the paramagnetic–ferromagnetic transition. For the $Pr_{0.55}Sr_{0.45}Mn_{1-x}Cr_xO_3$ series ($x = 0.0$, 0.05, 0.1, and 0.15), the magnetization *versus* temperature $M(T)$ curves provide important information on their magnetic behavior. These compounds show a change from a paramagnetic (PM) state to a ferromagnetic (FM) state as the temperature decreases. The key parameter known as the Curie temperature (T_C) indicates the temperature at which a material changes from a paramagnetic state to a ferromagnetic state. The Curie temperatures (T_C) were determined from the minimum value of the dM/dT *versus* T curves (refer to the inset of Fig. 2), and the T_C values for the $Pr_{0.55}Sr_{0.45}Mn_{1-x}Cr_xO_3$ series are shown to decrease as the Cr concentration increases: for $x = 0.0$, 0.05, 0.10, and 0.15, T_C (K) = 300 K, 292 K, 286 K and 275 K. This pattern implies that the ferromagnetic interactions are weakened when Mn is replaced with Cr in the lattice, which lowers the Tc, similarly in the literature, that is confirmed in the work of A. K. Saw *et al.*[67] and other work.[68] Furthermore, when Cr is substituted in Cr-doped manganites, the magnetism in the FM region decreases. A qualitative explanation for the decline in T_C and magnetization with the increase in chromium concentration is the decrease in the Mn^{3+}/Mn^{4+} ratio. This action increases the SE Super exchange antiferromagnetic state by reducing the Mn^{3+}/Mn^{4+} couples that cause DE Double exchange ferromagnetism and introducing a small amount of Mn^{3+}/Mn^{3+}, Mn^{4+}/Mn^{4+}, Cr^{3+}/Cr^{3+}, and Mn^{3+}/Cr^{3+} couples.[69]

The magnetization isotherms ($M(H)$) recorded for all compounds in magnetic fields equal to 5 T over a broad temperature range of 240–320 K demonstrate that, below the Curie temperature, magnetization increases significantly in weak applied fields until approaching saturation for applied fields ($\mu_0H = 1$ T). Fig. 3(a)–(d) display the usual magnetization isotherm shape for $x = 0.0$, 0.05, 0.1, and 0.15.

As the temperature decreases, the saturation magnetization increases. The purely ferromagnetic behavior of the samples at low temperatures is confirmed by this result. Important information on the magnetic characteristics and phase transitions of manganites is provided by the magnetization *versus* magnetic field $M(H)$ measurements. The nature of the magnetic ordering and the transitions between various magnetic phases are revealed by these observations. For example, the $M(H)$ curves in $Pr_{0.55}Sr_{0.45}Mn_{1-x}Cr_xO_3$ ($x = 0.00$, 0.05, 0.1, and 0.15) show a second-order ferromagnetic (FM)-to-paramagnetic (PM) phase

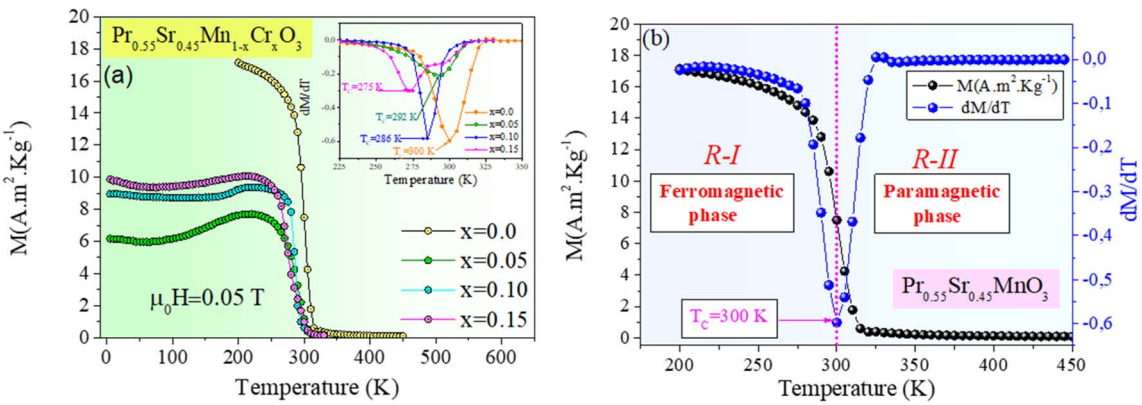

Fig. 2 (a) Temperature dependence of magnetization for the $Pr_{0.55}Sr_{0.45}Mn_{1-x}Cr_xO_3$ ($x = 0$, $x = 0.05$, $x = 0.1$ and $x = 0.15$) samples. Inset: dM/dT *versus* temperature curves of the samples. (b) Temperature dependence of magnetization measured at magnetic field (μ_0H) = 0.05 T for the $Pr_{0.55}Sr_{0.45}MnO_3$ sample and the dM/dT *versus* temperature curves.

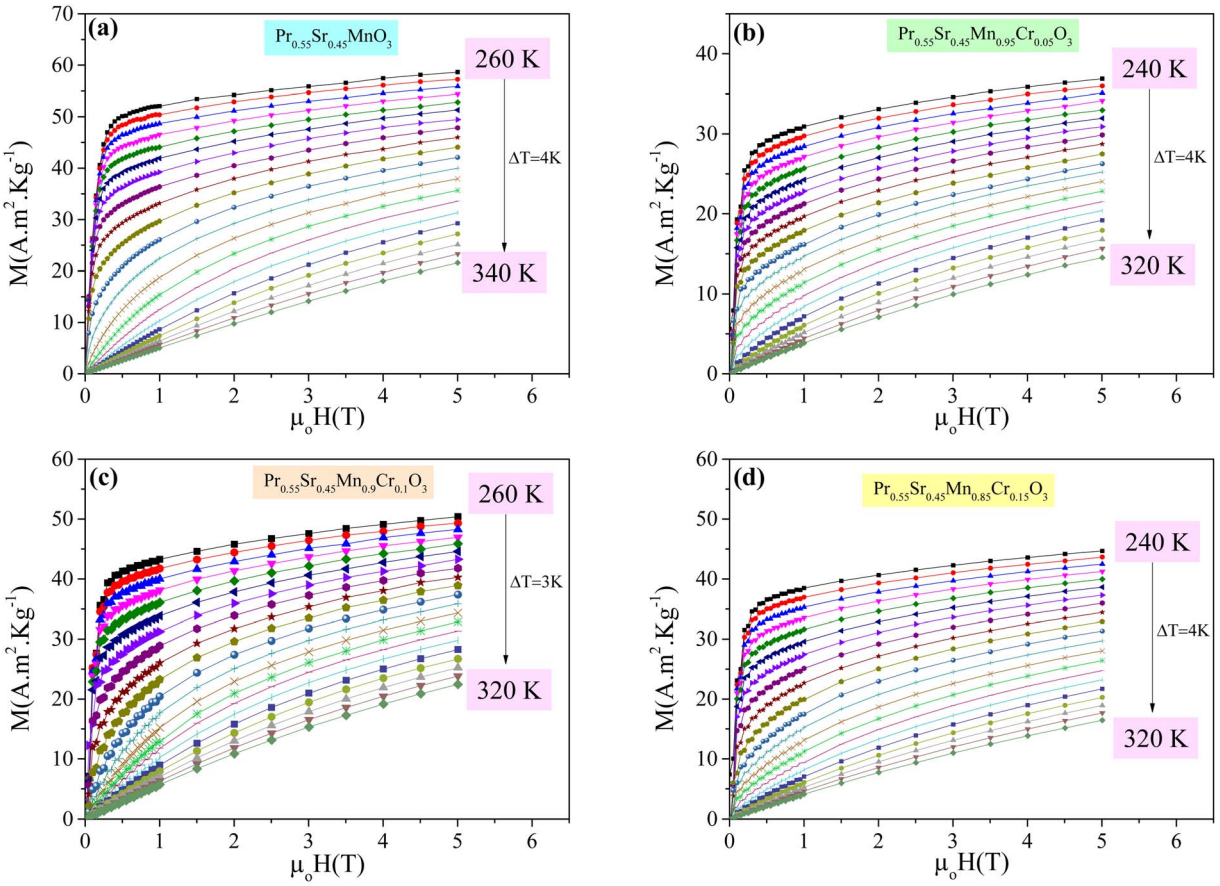

Fig. 3 Isothermal magnetization patterns the for $Pr_{0.55}Sr_{0.45}Mn_{1-x}Cr_xO_3$ ((a) $x = 0$, (b) $x = 0.05$, (c) $x = 0.1$ and (d) $x = 0.15$) samples at various temperatures.

transition, where the Curie temperature (T_C) decreases with the increase in Cr-doped concentration. Similarly, the $M(H)$ measurements reveal a second-order PM-to-FM transition in $Pr_{0.67}Sr_{0.33}Mn_{1-x}M_xO_3$ ($0.0 < x \leq 0.09$) in the study by A. Dhahri *et al.*[70] These findings are also essential for comprehending the magnetic interactions and the possible uses of the materials in magnetic refrigeration and other technologies.

3.3 Critical behavior

The analysis of the Arrott curve makes it possible to understand the critical behavior at the critical point. The magnetic equation of state for a system that adheres to the theory of the average field (MFT) is as follows:

$$\frac{H}{M} = A + BM^2. \quad (1)$$

The order of the magnetic phase transition is revealed by a thorough analysis of $M(H)$ isotherms. From the $M(H)$ isotherms near T_C, we inferred the Arrott plots ($M^{1/\beta}$ *vs.* $(\mu_0 H/M)^{1/\gamma}$), which are shown in Fig. 4(a)–(d). Banerjee criterion[71] states that a first-order or second-order magnetic phase transition is indicated by a negative or positive slope of Arrott curves. The results of M^2 against $\mu_0 H/M$ graphs for $Pr_{0.55}Sr_{0.45}Mn_{1-x}Cr_xO_3$ reveal the second-order FM-to-PM phase transition, with a positive slope in all cases throughout the entire M^2 range, and the values of exponents β and γ are 0.5 and 1, respectively, as expected from the mean field theory. The Curie temperatures (T_C) determined from the Arrott plots coincide with those obtained from the low-field magnetization curves ($M(T)$) for all compounds.

Fig. 5 shows the temperature dependence of the spontaneous magnetization (M_{sp}) deduced from the $M(H)$ curves and the inverse of the susceptibility ($1/\chi$) as a function of temperature for the $Pr_{0.55}Sr_{0.45}MnO_3$ sample. In the paramagnetic phase ($T > T_C$), this sample exhibits linear inverse susceptibility behavior. $X = C/(T - \theta_P)$, where θ_P is the Curie constant and C is the Curie–Weiss temperature. For $x = 0.0$, the θ_P value is determined to be 303 K. The presence of a ferromagnetic exchange interaction between the closest neighbors is indicated by the positive value of θ_P. The resultant value is marginally above the Curie temperatures. Short-range magnetic correlations above the Curie temperature are linked to this material-dependent differential, which is suggestive of magnetic inhomogeneity.[72] For $x = 0.0$, the critical exponent β is determined to be 0.362, indicating that all of our samples exhibit ferromagnetic activity at low temperatures. The ferromagnetic condition described for manganites[63,72,73] is in good agreement with this value.

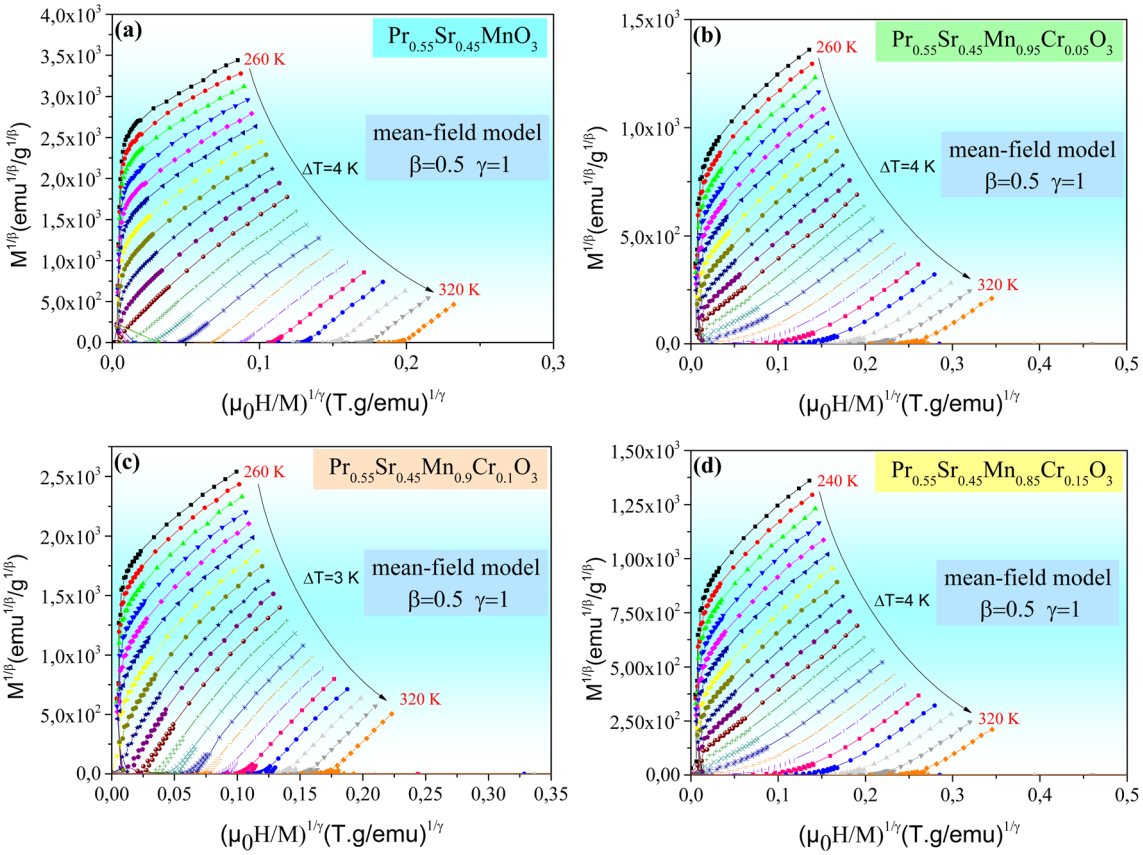

Fig. 4 Arrott plots ($(M^{1/\beta}$ *vs.* $\mu_0H/M)^{1/\gamma}$) with $\beta = 0.5$ and $\gamma = 1$, of the $Pr_{0.55}Sr_{0.45}Mn_{1-x}Cr_xO_3$ ((a) $x = 0$, (b) $x = 0.05$, (c) $x = 0.1$ and (d) $x = 0.15$) compounds.

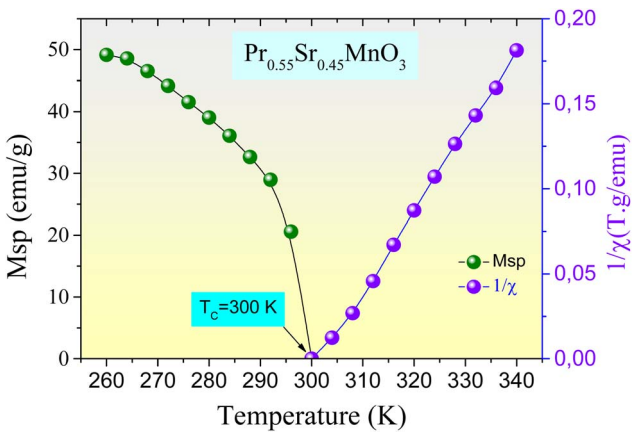

Fig. 5 Spontaneous magnetization (M_{sp}) and the inverse of susceptibility $1/\chi$ as a function of temperature for the $Pr_{0.55}Sr_{0.45}MnO_3$ compound.

3.4 Magnetocaloric measurements

The thermodynamic theory states that the magnetic entropy change caused by the magnetic field variation from 0 to H_{max} is as follows:[74]

$$\Delta S_M(T,H) = S_M(T,H) - S_M(T,0) = \int \frac{dM(T,H)}{dT} dH \quad (2)$$

Using Maxwell's relation:

$$\left(\frac{\partial M}{\partial T}\right)_H = \left(\frac{\partial S}{\partial H}\right)_T. \quad (3)$$

The following expression can be obtained:

$$\Delta S_M\ (T,H) = \int_0^{H_{max}} \left(\frac{\partial M}{\partial T}\right)_H dH. \quad (4)$$

Eqn (4) states that the magnetic entropy change reaches its highest during the magnetic transition phase. The magnetic entropy change was calculated approximately using the numerical formula employing isothermal magnetization data in small discrete field and temperature intervals:[75]

$$\Delta S_M\ (T,H) = \sum \left(\frac{M_i - M_{i+1}}{T_{i+1} - T_i}\right) \Delta H_i, \quad (5)$$

where M_i and M_{i+1} are the experimental magnetization values obtained at the temperatures T_i and T_{i+1}, respectively, in an applied magnetic field (H_i). The magnetic entropy changes $|\Delta S_M|$ of $Pr_{0.55}Sr_{0.45}Mn_{1-x}Cr_xO_3$ samples as a function of temperature under various magnetic applied field variations are plotted in Fig. 6(a)–(d). The magnetic entropy change increases

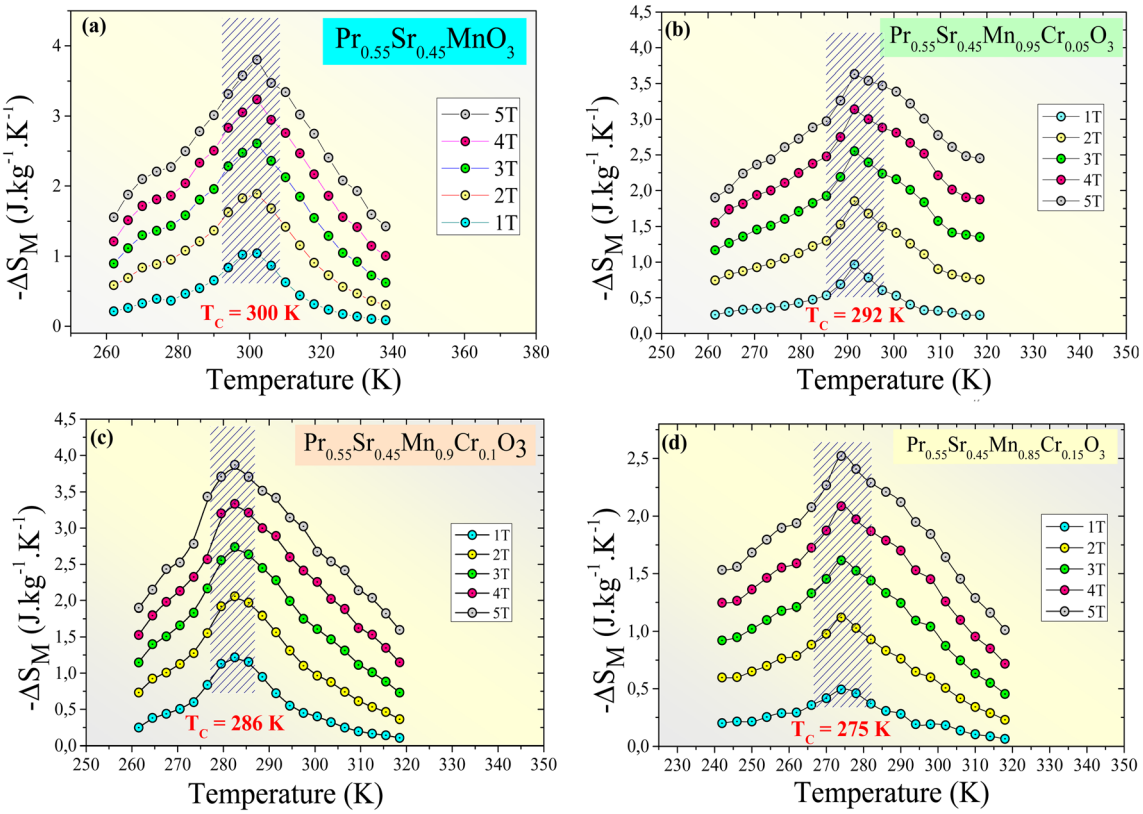

Fig. 6 Magnetic entropy change ($-\Delta S_M$) *vs.* T around the Curie temperature (T_C) for the $Pr_{0.55}Sr_{0.45}Mn_{1-x}Cr_xO_3$ ((a) $x = 0$, (b) $x = 0.05$, (c) $x = 0.1$ and (d) $x = 0.15$) compounds.

with temperature and reaches a maximum near the Curie temperature.

The $-\Delta S_M$ value exhibits a broad positive peak around T_C (normal MCE) for all samples. The maximum values of the magnetic entropy change ($|\Delta S_M^{max}|$) are 3.8 J kg^{-1} K^{-1}, 3.63 J kg^{-1} K^{-1}, 3.87 J kg^{-1} K^{-1} and 2.55 J kg^{-1} K^{-1} in a magnetic field change of 5 T for $x = 0.0$, $x = 0.05$, $x = 0.1$ and $x = 0.15$, respectively. The relative cooling power (RCP)[76–78] is evaluated as follows:

$$RCP = -\Delta S_M(T,H) \times \delta T_{FWHM}, \quad (6)$$

where δT_{FWHM} is the full width at half maximum of $-\Delta S_M$ *versus* temperature.[79–81] For our samples, the RCP values are, respectively, 247 J kg^{-1}, 254.1 J kg^{-1}, 205.1 J kg^{-1} and 201 J kg^{-1} at 5 T for $x = 0.0$, $x = 0.05$, $x = 0.1$ and $x = 0.15$. Despite having the lowest $|\Delta S_M^{max}|$, the composition of 5% of chromium-doped manganese seems to be the most promising for magnetic refrigeration applications because of its high RCP value. For cooling cycles to be effective, entropy change and temperature range must be balanced. As seen in Fig. 7, the delta $|\Delta S_M^{max}|$ values obtained and the RCP values computed using eqn (6) are plotted *versus* $\mu_0 H$.

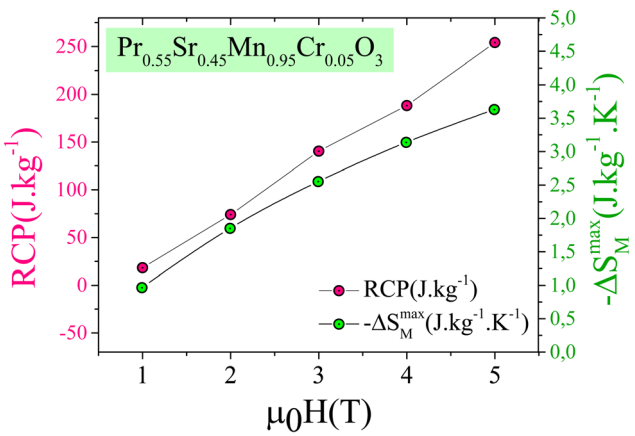

Fig. 7 Relation of the maximum entropy changes ($-\Delta S_M^{max}$) and relative cooling power (RCP) with $\mu_0 H$ for the $Pr_{0.55}Sr_{0.45}MO_3$ compound.

It was evident that at T_C, the relative cooling power (RCP) and maximum entropy change ($|\Delta S_M^{max}|$) are both proportional to $\mu_0 H$ (Table 2). RCP is a field-dependent variable, as evidenced by its trend with μ_0H. Our sample RCP (5% of chromium) value of 254.1 J kg^{-1} is 58% of Gd, which is the industry standard for refrigeration[75] materials with high δT_{FWHM}, and RCP values can operate over a wide temperature range and have a large cooling capacity. Magnetic refrigeration works well with these materials.[82,83]

A comparison of the magnetocaloric performance of the benchmark material Gd under an applied magnetic field of 5 T is shown in Table 3. The Curie temperatures (T_C) of all the samples remain near room temperature, which is advantageous for magnetic refrigeration applications. As would be predicted

Table 2 Summary of $-\Delta S_M^{max}$, the Curie temperature T_C and relative cooling power (RCP) a values of $Pr_{0.55}Sr_{0.45}Mn_{1-x}Cr_xO_3$ with $x = 0.0$, 0.05, 0.1, and 0.15

X	0	0.05	0.10	0.15
T_C (K)	300	292	286	275
$-\Delta S_M^{max}$(J kg^{-1} K^{-1})	3.80	3.63	3.87	2.55
δT_{FWHM}	65	70	53	79
RCP (J kg^{-1})	247	254.1	205.1	201

Table 3 Collected data for the Curie temperature (T_C), $-\Delta S_M^{max}$, and RCP of our studied compounds and the reference material Gd

x	T_C (K)	ΔH (T)	$-\Delta S_M^{max}$(J kg^{-1} K^{-1})	RCP (J kg^{-1})	Ref.
$x = 0$	300	5	3.8	247	This work
$x = 0.05$	292	5	3.63	254.1	This work
$x = 0.1$	286	5	3.87	205.1	This work
$x = 0.15$	275	5	2.55	201	This work
Gd	294	5	10.2	410	75

for perovskite manganites, the maximum magnetic entropy change ($-\Delta S_M^{max}$) values of the examined compounds, which range from 2.55 to 3.87 J kg^{-1} K^{-1}, are lower than those of Gd (10.2 J kg^{-1} K^{-1}). However, the RCP values, especially for $x = 0$ and $x = 0.05$, approach considerable values (247 and 254.1 J kg^{-1}, respectively), but they are still quite similar to Gd (410 J kg^{-1}). This suggests that the wider operating temperature range of manganites helps to maintain competitive RCP values even though the entropy change is less. These findings verify that the investigated compounds are viable low-cost substitutes for Gd in magnetic refrigeration close to room temperature.

The temperature interval is primarily responsible for the higher RCP values despite the lower ΔS_M^{max} values. Because of the gradual nature of the magnetic transition and Cr-related magnetic disorder, this rise in δT_{FWHM} makes up for the decreased peak entropy change and improves the overall refrigeration efficiency.

Numerous methods for figuring out the order of magnetic phase transitions have been proposed in the literature.[71,84] One of these is to use the relation $\Delta S_M(H,T) \approx aH^n$, where a is a constant and n is an exponent related to magnetic order, to examine the field dependence of the samples' MCE.[85–87] Important details regarding the type of magnetic phase transition in the investigated materials can be found by calculating the exponent values at specific temperatures. The logarithmic derivative of experimental data can be used to determine the exponent n at a specific temperature and magnetic field $\Delta S_M(H,T)$[85] as follows:

$$n(T,\ H) = \frac{d\ln(\Delta S_M(T,H))}{d\ln(H)}. \quad (7)$$

The Curie–Weiss rule causes the n values to approach $n = 2$ at high temperatures in the paramagnetic phase (over the T_C).[86] In the ferromagnetic phase, n typically has a value that tends to be $n = 1$ at temperatures well below the transition point. The value of n changes according to the kind of phase transition (first- or second-order) of the material within a crucial temperature range surrounding the Curie temperature.

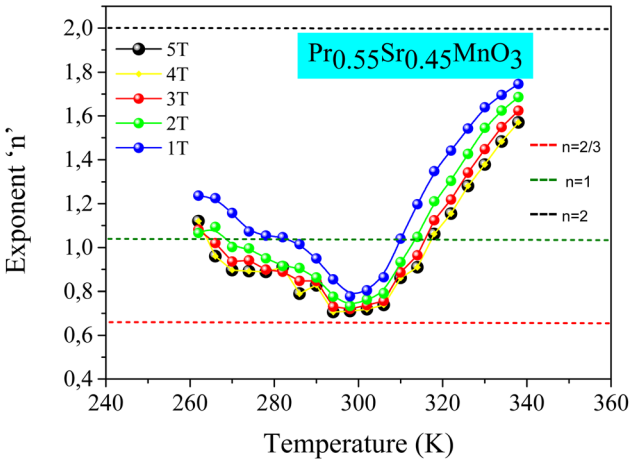

Fig. 8 Temperature dependence of the exponent ($n(T)$) of the magnetic entropy change ($-\Delta S_M$) for several applied magnetic field values of $Pr_{0.55}Sr_{0.45}MO_3$.

Previous investigation has demonstrated that a quantitative criterion of $n > 2$ close to the transition temperature $T = T_C$ could be interpreted as a first-order magnetic phase transition of the material. It has also been demonstrated that this criterion could be successfully applied to a variety of magnetocaloric materials in order to identify the type of magnetic phase transition.[87]

Fig. 8 illustrates the $Pr_{0.55}Sr_{0.45}MnO_3$ compound temperature dependency of exponent n under various magnetic fields ($n(T)$). The sample exponent n tends to approach 1 at temperatures significantly below the Curie temperature (ferromagnetic region). The exponent n tends to 2 for temperatures greater than T_C (paramagnetic zone). This behavior for exponent n is typically explained by a second-order phase transition. As the temperature drops near the transition temperature, a fall in n is seen, with a minimum value at the Curie temperature. Other magnetic materials with first- and second-order transitions have been reported to exhibit similar behaviors.[41,71,84–86,88]

4 Conclusions

In summary, this study focused on the structural, magnetic, and magnetocaloric characterisation of $Pr_{0.55}Sr_{0.45}Mn_{1-x}Cr_xO_3$ manganite compounds with $x = 0.0$, 0.05, 0.1, and 0.15, which were successfully elaborated using a solid–state reaction method. The crystalline structure was found to be orthorhombic, corresponding to the *Pnma* space group, and X-ray diffraction investigations verified the production of a single phase over the compositional range without any impurity phase.

For all the prepared compounds, magnetization measurements as a function of temperature and applied field consistently showed a magnetic phase transition from the

ferromagnetic (FM) state to the paramagnetic (PM) state. It is remarkable that this transition was found to be of second order. It was discovered that the Curie temperature (T_C), which decreased from 300 K to 275 K over the examined substitution period, could be efficiently modulated by gradually adding chromium in place of manganese. The crucial impact of the Cr^{3+} ion on the magnetic exchange processes inside the crystal lattice is shown by this dependence.

Using isothermal magnetization data and the Maxwell thermodynamic laws, the magnetocaloric effect (MCE) was thoroughly examined. The outcomes for a 5 T change in the magnetic field are very encouraging. For the $x = 0.1$ composition, the highest magnetic entropy change ($-\Delta S_M^{max}$) was found to peak at 3.87 J kg^{-1} K^{-1}. More significantly, the $Pr_{0.55}Sr_{0.45}Mn_{0.95}Cr_{0.05}O_3$ sample had the highest relative cooling power (RCP) value, measuring 254.1 J kg^{-1}.

Considering that its RCP value is roughly 58% of that of pure gadolinium, an accepted industrial measurement, this performance places the material with $x = 0.05$ in a very promising category for magnetic refrigeration applications. In conclusion, the $Pr_{0.55}Sr_{0.45}Mn_{1-x}Cr_xO_3$ family of manganites are an attractive class of magnetocaloric materials for the fabrication of effective and eco-friendly magnetic cooling devices, especially because the chromium concentration can be used to adjust the operating temperature.

Conflicts of interest

There are no conflicts of interest to declare.

Data availability

The data that support the findings of this study are available from the corresponding author upon reasonable request.

References

1 Y. Tokura, *Rep. Prog. Phys.*, 2006, **69**, 797–851.
2 M. H. M.-H. Phan, S. C. Yu and N. H. Hur, *J. Appl. Phys. Lett.*, 2005, **86**, 072504.
3 A. P. Ramirez, *J. Phys. Condens. Matter*, 1997, **9**, 8171–8199.
4 E. Dagotto, J. Burgy and A. Moreo, *Solid State Commun.*, 2003, **126**, 9–22.
5 H. Li, S. Li, Y. Wang, H. Sarvari, P. Zhang, M. Wang and Z. Chen, *Sol. Energy*, 2016, **126**, 243–251.
6 E. Warburg, *Ann. Phys.*, 1881, **249**, 141–164.
7 W. Chen, L. Y. Nie, W. Zhong, Y. J. Shi, J. J. Hu, A. J. Li and Y. W. Du, *J. Alloys Compd.*, 2005, **395**, 23–25.
8 S. K. Çetin, M. Acet, M. Güneş, A. Ekicibil and M. Farle, *J. Alloys Compd.*, 2015, **650**, 285–294.
9 F. Anwar, B. Ahmed and H. Koo, *J. Alloys Compd.*, 2014, **617**, 893–898.
10 W. Tang, Z. Mao and Z. Zou, *J. Magn. Magn Mater.*, 2020, **515**, 167283.
11 F. B. Jemaa, S. Mahmood, M. Ellouze, E. K. Hlil, F. Halouani, I. Bsoul and M. Awawdeh, *Solid State Sci.*, 2014, **37**, 121–130.
12 M. Hsini, L. Ghivelder and F. Parisi, *J. Magn. Magn Mater.*, 2021, **535**, 168059.
13 I. Z. Al-Yahmadi, A. Gismelseed, H. M. Widatallah, F. Bzour, F. A. Ma'Mari, A. Al-Rawas and M. ElZain, *Mater. Chem. Phys.*, 2024, **329**, 130109.
14 A. O. Ayaş, S. K. Çetin, G. Akça, M. Akyol and A. Ekicibil, *Mater. Today Commun.*, 2023, **35**, 105988.
15 I. Z. Al-Yahmadi, A. AlSaadi, A. Gismelseed, F. A. Ma'Mari, H. M. Widatallah, F. Bzour and R. A. Busaidi, *J. Alloys Compd.*, 2025, **1042**, 183941.
16 Z. Aydi, R. Dhahri, S. Kammoun, E. Dhahri, E.-K. Hlil and E. López-Lago, *J. Alloys Compd.*, 2025, **1032**, 180656.
17 P. Amalthi, J. J. Vijaya, L. J. Kennedy, A. Mustafa, M. Bououdina, K. P. Shinde and D. H. Kim, *Ceram. Int.*, 2022, **48**, 36880–36887.
18 S. Soumya, B. Sattibabu, T. D. Rao, R. K. Gurazada and A. K. Bhatnagar, *Ceram. Int.*, 2025, **51**, 63102–63111.
19 A. Dhahri, Y. Moualhi, F. Elleuch, E. Dhahri and N. Abdelmoula, *J. Phys. Chem. Solid.*, 2025, **209**, 113328.
20 P. Z. Z. Nehan, B. Kurniawan, D. R. Munazat, O. Vitayaya, M. Naibaho, T. Sudiro, M. T. E. Manawan, D. Darminto and H. Nojiri, *J. Alloys Compd.*, 2025, **1020**, 179467.
21 A. G. Gamzatov, A. B. Batdalov, N. Z. Abdulkadirova, A. M. Aliev, V. V. Khovaylo, T. D. Thanh, N. T. Dung and S.-c. Yu, *J. Alloys Compd.*, 2023, **964**, 171330.
22 W. Mo, J. Wang, G. Yuan, D. Cao and G. Bai, *Mater. Today Commun.*, 2025, **44**, 111933.
23 G. Akça, S. K. Çetin and A. Ekicibil, *Ceram. Int.*, 2017, **43**, 15811–15820.
24 X. Jin, H. Ma, Q. Li, J. Xu, J. Zhao, T. O and J. Huang, *iScience*, 2025, **28**, 112533.
25 N. Mtiraoui, N. Dhouibi, J. Dhahri and O. Toulemonde, *J. Solid State Chem.*, 2020, **294**, 121847.
26 X. Bao, J. Wang, X. Wu, C. He, H. Luo, Q. Bai, V. Bao, Y. Bai, J. Liu and S. Zhao, *Phys. B Condens. Matter*, 2023, **671**, 415410.
27 M. Lassri, M. Sajieddine, A. Elouafi, A. E. Hachmi, S. E. Ouahbi and R. Moubah, *J. Rare Earths*, 2023, **42**, 1724–1729.
28 G. Kadim and R. Masrour, *Ceram. Int.*, 2024, **51**, 147–153.
29 R. Hamdi, S. Boulfrad, S. S. Hayek, A. Samara, S. A. Mansour and Y. Haik, *Inorg. Chem. Commun.*, 2023, **158**, 111589.
30 M. Zarifi, P. Kameli, T. Raoufi, A. G. Varzaneh, D. Salazar, M. I. Nouraddini, L. Kotsedi and M. Maaza, *J. Magn. Magn Mater.*, 2019, **494**, 165734.
31 A. Mleiki, S. Othmani, W. Cheikhrouhou-Koubaa, M. Koubaa, A. Cheikhrouhou and E. K. Hlil, *J. Alloys Compd.*, 2015, **648**, 1043–1050.
32 J. Fan, L. Pi, L. Zhang, W. Tong, L. Ling, B. Hong, Y. Shi, W. Zhang, D. Lu and Y. Zhang, *Appl. Phys. Lett.*, 2011, **98**, 072508.
33 A. Mleiki, S. Othmani, W. Cheikhrouhou-Koubaa, A. Cheikhrouhou and E. K. Hlil, *J. Alloys Compd.*, 2016, **688**, 1214–1224.
34 C. Zener, *Phys. Rev.*, 1951, **82**, 403–405.
35 M. W. Shaikh and D. Varshney, *Mater. Sci. Semicond. Process.*, 2014, **27**, 418–426.

36 S. Vadnala, T. D. Rao, P. Pal and S. Asthana, *Phys. B Condens. Matter*, 2014, **448**, 277–280.
37 A. Hassen, *J. Kor. Phys. Soc.*, 2008, **52**, 98–105.
38 A. Selmi, R. M'nassri, W. Cheikhrouhou-Koubaa, N. C. Boudjada and A. Cheikhrouhou, *J. Alloys Compd.*, 2014, **619**, 627–633.
39 S. K. Barik, C. Krishnamoorthi and R. Mahendiran, *J. Magn. Magn Mater.*, 2010, **323**, 1015–1021.
40 M. Khelifi, R. M'nassri, A. Selmi, H. Rahmouni, K. Khirouni, N. C. Boudjada and A. Cheikhrouhou, *J. Magn. Magn Mater.*, 2016, **423**, 20–26.
41 Y. Moualhi, R. M'nassri, M. M. Nofal, H. Rahmouni, A. Selmi, M. Gassoumi, N. Chniba-Boudjada, K. Khirouni and A. Cheikrouhou, *Eur. Phys. J. Plus*, 2020, **135**, 809.
42 H. Nakatsugawa, M. Saito and Y. Okamoto, *J. Electron. Mater.*, 2017, **46**, 3262–3272.
43 K. Snini, R. Abidi, A. Ekicibil, M. Ellouze and L. E. Mir, *J. Mater. Sci. Mater. Electron.*, 2021, **32**, 22330–22341.
44 A. Selmi, M. Khelifi, H. Rahmouni, R. M'nassri, K. Khirouni, N. C. Boudjada and A. Cheikhrouhou, *J. Mater. Sci. Mater. Electron.*, 2016, **28**, 1901–1908.
45 M. R. Laouyenne, M. Baazaoui, F. Aouaini, B. Basha and K. S. Al-Mugren, *J. Supercond. Nov. Magnetism*, 2025, **38**, 209.
46 R. Usnilawaty and B. Kurniawan, *J.Fis. dan Apl.*, 2025, **13**, 153.
47 A. Selmi, R. M'nassri, W. Cheikhrouhou-Koubaa, N. C. Boudjada and A. Cheikhrouhou, *Ceram. Int.*, 2015, **41**, 7723–7728.
48 B. Dey, A. Basu, S. Pal and S. Kumar, *EPJ Web Conf.*, 2025, **325**, 01001.
49 A. Selmi, A. Bettaibi, H. Rahmouni, R. M'nassri, N. C. Boudjada, A. Chiekhrouhou and K. Khirouni, *Ceram. Int.*, 2015, **41**, 11221–11227.
50 M. M. Alanazi, M. Baazaoui and F. Aouaini, *J. Supercond. Nov. Magnetism*, 2022, **35**, 1613–1619.
51 S. Mahjoub, R. M'nassri, M. Baazaoui, M. M. Nofal, E. M. A. Dannoun, E. K. Hlil and M. Oumezzine, *J. Mater. Sci. Mater. Electron.*, 2021, **32**, 6094–6109.
52 M. Oumezzine, S. Hcini, M. Baazaoui, H. B. Sales, I. M. G. D. Santos and M. Oumezzine, *J. Alloys Compd.*, 2013, **571**, 79–84.
53 C. P. Reshmi and A. R. Ramesh, *Phys. B Condens. Matter*, 2025, **714**, 417486.
54 Z. Xie, X. Zheng, W. He, M. Feng, C. Xu and Z. Zou, *Ceram. Int.*, 2024, **51**, 10026–10040.
55 W. Zhang, Y. Fu, C. Qin, Q. Wu and Y. Liang, *J. Phys. Conf.*, 2025, **3102**, 012012.
56 Y. L. Chang, Q. Huang and C. K. Ong, *J. Appl. Phys.*, 2002, **91**, 789–793.
57 M. Baazaoui, S. Zemni, M. Boudard, H. Rahmouni, A. Gasmi, A. Selmi and M. Oumezzine, *Mater. Lett.*, 2009, **63**, 2167–2170.
58 A. J. Millis, P. B. Littlewood and B. I. Shraiman, *Phys. Rev. Lett.*, 1995, **74**, 5144–5147.
59 Y. A. Izyumov and Y. N. Skryabin, *Phys. Usp.*, 2001, **44**, 109–134.
60 T. D. Thanh, T. A. Ho, T. V. Manh, T. L. Phan and S.-C. Yu, *IEEE Trans. Magn.*, 2014, **50**, 1–4.
61 W. C.-R. Koubaa, M. Koubaa and A. Cheikhrouhou, *Phys. Procedia*, 2009, **2**, 989–996.
62 A. Selmi, W. Cheikhrouhou-Koubaa, M. Koubaa and A. Cheikhrouhou, *J. Supercond. Nov. Magnetism*, 2012, **26**, 1421–1428.
63 H. M. Rietveld, *J. Appl. Crystallogr.*, 1969, **2**, 65–71.
64 T. Roisnel, J. Rodriguez-Carvajal, *Computer Program FULLPROF, LLB-LCSIM*, May, 2003.
65 J. A. Alonso, M. J. Martínez-Lope, M. T. Casais and M. T. Fernández-Díaz, *Inorg. Chem.*, 2000, **39**, 917–923.
66 Young, R. A., *The Rietveld Method*, Oxford, online edn, Oxford Academic, 1993,.
67 A. K. Saw, S. Hunagund, R. L. Hadimani and V. Dayal, *Mater. Today Proc.*, 2020, **46**, 6218–6222.
68 F. Zdiri, J. M. Alonso, T. Mnasri, P. De la Presa, I. Morales, J. L. Martínez, R. B. Younes and P. Marin, *Materials*, 2023, **16**, 1573.
69 A. Chanda and R. Mahendiran, *IEEE Trans. Magn.*, 2018, **54**, 1–5.
70 A. Dhahri, Ja. Dhahri, S. Hcini, N. Talbi, E. K. Hlil, M. Oumezzine and K. Khirouni, *Appl. Phys. A*, 2015, **120**, 247–253.
71 B. K. Banerjee, *Phys. Lett.*, 1964, **12**, 16–17.
72 R. M'nassri, N. C. Boudjada and A. Cheikhrouhou, *J. Alloys Compd.*, 2014, **626**, 20–28.
73 R. M'nassri, W. Cheikhrouhou-Koubaa, N. Chniba-Boudjada and A. Cheikhrouhou, *J. Appl. Phys.*, 2013, **113**, 073905.
74 R. Cherif, E. K. Hlil, M. Ellouze, F. Elhalouani and S. Obbade, *J. Solid State Chem.*, 2014, **215**, 271–276.
75 K. A. Gschneidner and V. K. Pecharsky, *Annu. Rev. Mater. Sci.*, 2000, **30**, 387–429.
76 P. Gorria, J. L. S. Llamazares, P. Álvarez, M. J. Pérez, J. S. Marcos and J. A. Blanco, *J. Phys. D Appl. Phys.*, 2008, **41**, 192003.
77 N. Gayathri, A. K. Raychaudhuri, S. K. Tiwary, R. Gundakaram, A. Arulraj and C. N. R. Rao, *Phys. Rev. B Condens. Matter*, 1997, **56**, 1345–1353.
78 M. A. Señarís-RodrÍGuez and J. B. Goodenough, *J. Solid State Chem.*, 1995, **118**, 323–336.
79 V. S. Kolat, T. Izgi, A. O. Kaya, N. Bayri, H. Gencer and S. Atalay, *J. Magn. Magn Mater.*, 2009, **322**, 427–433.
80 A. D. Souza, M. Vagadia and M. D. Daivajna, *Appl. Phys. A*, 2021, **127**, 677.
81 A. Selmi, R. M'nassri, W. Cheikhrouhou-Koubaa, N. C. Boudjada and A. Cheikhrouhou, *Ceram. Int.*, 2015, **41**, 10177–10184.
82 M. Földeàki, R. Chahine and T. K. Bose, *J. Appl. Phys.*, 1995, **77**, 3528–3537.
83 V. K. Pecharsky and K. A. Gschneidner Jr, *Phys. Rev. Lett.*, 1997, **78**, 4494–4497.
84 C. P. Bean and D. S. Rodbell, *Phys. Rev.*, 1962, **126**, 104–115.
85 V. Franco, J. S. Blázquez, B. Ingale and A. Conde, *Annu. Rev. Mater. Res.*, 2012, **42**, 305–342.

86 J. Y. Law, V. Franco, L. M. Moreno-Ramírez, A. Conde, D. Y. Karpenkov, I. Radulov, K. P. Skokov and O. Gutfleisch, *Nat. Commun.*, 2018, **9**, 2680.
87 R. M'nassri, M. M. Nofal, P. De Rango and N. Chniba-Boudjada, *RSC Adv.*, 2019, **9**, 14916–14927.
88 V. S. Kumar, R. Mahendiran and B. Raveau, *IEEE Trans. Magn.*, 2010, **46**, 1652–1655.